Fluorine-doped nanocrystalline SnO₂ powders prepared via a single molecular precursor method as anode materials for Li-ion batteries

Hyung-Wook Ha[a], Keon Kim[a],*, Mervyn de Borniol[b], Thierry Toupance[b],**

[a]*Division of Chemistry and Molecular Engineering, Korea University, Seoul 136-701, South Korea*
[b]*Laboratoire de Chimie Organique et Organométallique, UMR 5802 CNRS, University Bordeaux 1, 351 Cours de la Libération,
F-33405 Talence Cédex, France*

Abstract

Fluorine-doped nanocrystalline tin dioxide materials (F:SnO₂) have been successfully prepared by the sol–gel process from a single molecular precursor followed by a thermal treatment at 450–650 °C. The resulting materials were characterized by FTIR spectroscopy, powder X-ray diffraction, nitrogen adsorption porosimetry (BET) and transmission electron microscopy (TEM). The mean particle size increased from 5 to 20 nm and the specific surface area decreased from 123 to 37 m²/g as the temperature of heat treatment was risen from 450 to 650 °C. Fluorine-doped nanocrystalline SnO₂ exhibited capacity of 560, 502, and 702 mA h/g with 48%, 50%, and 40% capacity retention after 25 cycles between 1.2 V and 50 mV at the rate of 25 mA/g, respectively. In comparison, commercial SnO₂ showed an initial capacity of 388 mA h/g, with only 23% capacity retention after 25 cycles.
© 2005 Elsevier Inc. All rights reserved.

Keywords: Fluorine; Tin dioxide; Li batteries; Anode material; Nanoparticles

1. Introduction

Tin dioxide, an *n*-type wide band gap semiconductor showing high chemical and mechanical stabilities, demonstrates unique photo-electronic properties and good sensitivity towards gases [1–4]. It finds therefore widespread applications as gas sensors [5] and as oxide material in dye-sensitized solar cell [6]. Over the past decade, Li-ion batteries using a graphite anode have received a considerable interest for uses in a variety of electronic devices. Notwithstanding their successful commercialization, various new anode materials have been tested out to overcome the initial capacity of graphite (372 mA h/g) which is less than one-tenth of that of lithium metal (3860 mA h/g). Many efforts have therefore been made to find out alternative anode materials to replace graphite in lithium-

ion batteries. In this context, tin-based oxide material such as SnO₂ showed higher specific capacity as anode active materials than carbonaceous materials. Nonetheless, a large irreversible capacity loss at the first cycle due to the formation of a Li–Sn alloy reaction was generally reported [7,8] which has prevented any practical application for SnO₂ as anode material. Many studies have been devoted to the improvement of both electrochemical performance and stability of SnO₂-based materials [9,10]. One of the strategies to improve the conductivity and electrochemical reversibility is doping the SnO₂–graphite composite with Cl, Sb, Mo or F atoms [11–16]. Among these elements, the fluorine is known to be the most efficient doping agent for SnO₂ to achieve the highest electrical conductivity, i.e. $\sim 5 \times 10^3 \, \Omega^{-1} \, cm^{-1}$, for an optimum atomic F/Sn ratio of $\sim 3\%$ [17]. In the field of lithium-ion battery, very small tin oxide particles are needed to obtain high capacity [18–20], which requires the preparation of nanosized SnO₂ particles.

Up to now, tin oxide nanoparticles were prepared by various different synthetic methods, such as precipitation, hydrothermal, solvothermal, gel-combustion or spray

---

*Corresponding author. Fax: +82 2 953 1172.
**Also to be corresponded to: Fax: +33 05 40 00 69 94
  E-mail addresses: kkim@korea.ac.kr (K. Kim),
t.toupance@lcoo.u-bordeaux1.fr (T. Toupance).

pyrolysis method [21–27]. The sol–gel method is one of the most promising synthetic method for nanoparticles of controlled size and morphology [28,29]. This method has recently been extended to the synthesis of nanocrystalline F-doped SnO_2 powders [30,31].

In this study, F-doped nanocrystalline SnO_2 powders were synthesized by the sol–gel route from a single molecular precursor and were characterized by different analytical techniques. Their electrochemical properties as an anode material for lithium battery have also been examined.

2. Experimental

Nanocrystalline F-doped SnO_2 powders were prepared by the sol–gel method from the fluoro(2-methylbutan-2-oxy)di(pentan-2,4-dionato)tin complex **1** [32] according to a previously reported procedure (Fig. 1) [30]. The gel obtained was first dried at 80 °C in vaccum and then calcined at 450, 550 or 650 °C in air atmosphere for 30 min. The samples are thus labelled G^T where T corresponds to the temperature of the thermal treatment. Elemental analyses have been performed in the Center of Chemical Analysis of the "Centre National de la Recherche Scientifique" (Vernaison, France). Short contact times to avoid titration of surface hydroxyl groups were used to estimate the water amount in the xerogel by the Karl–Fisher method. For sake of comparison, 40 nm sized commercial SnO_2 powder was purchased from Aldrich Chemicals (99.9%).

XRD patterns were recorded using a Rigaku DMAX-βA diffractometer equipped with a Cu target X-ray tube. The scan data were collected in the 2θ range of 15–70°. The step size was 0.020° with counting time of 0.4 s. Infrared red spectra (KBr pellets) were recorded in the absorption mode using a FTIR Perkin-Elmer spectrophotometer. The crystallite sizes were estimated from the half-height line broadening by applying the modified Scherrer formula $t = (0.9\lambda)/(\beta \cos \theta)$ where λ is the wavelength, θ is the Bragg angle and β is the angular half-width. Nitrogen adsorption isotherm (77 K) measurements were carried out by the static volumetric method using an ASAP2010 (Micromeritics) apparatus after degassing at 100 °C in vacuum. The pore size distribution was evaluated by the Barrett, Joyner, Halenda (BJH) method applied to the adsorption branch of the nitrogen adsorption–desorption isotherms. The morphology of the samples was determined by transmis-

sion electron microscopy (TEM) using a JEOL 2000X instrument.

The electrochemical properties of the powders were examined using a two-electrode electrochemical cell. A mixture of 20 mg of F-doped SnO_2 compounds and 12 mg of conductive binder (8 mg of teflonized acetylene black and 4 mg of graphite) was applied to an aluminium foil. The resulting electrodes were pressed and vacuum dried overnight at 120 °C. They were then assembled into Li test cells using lithium foil negative electrodes, porous PFTE films as separators, and an electrolyte of 1 M $LiPF_6$ in a 50:50 w/w polypropylene carbonate (PC) and diethyl carbonate (DEC) solution (TECHNO SEMICHEM Co., Ltd.). Cell assembly was performed in a glove box under a recirculating argon atmosphere. The cells were aged for at least 24 h after assembly before galvanostatically cycled between 50 mV and 1.2 V with the current density of 25 mA/g using a WBCS 3000 instrument.

3. Results and discussion

The XRD patterns of the dried xerogel precursor and the nanocrystalline F-doped SnO_2 powders are displayed in Fig. 2. For the dried xerogel precursor, no distinguishable peak could be detected revealing an amorphous state. After thermal treatment, several reflections appeared in the XRD patterns which were indexed with tetragonal symmetry
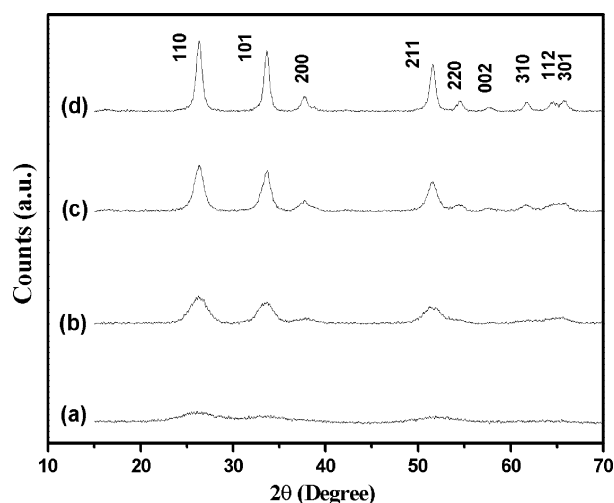
Fig. 2. XRD patterns of the (a) precursor and F-doped SnO_2 nanocrystallites samples calcined at (b) 450 °C, (c) 550 °C, (d) 650 °C for 30 min.
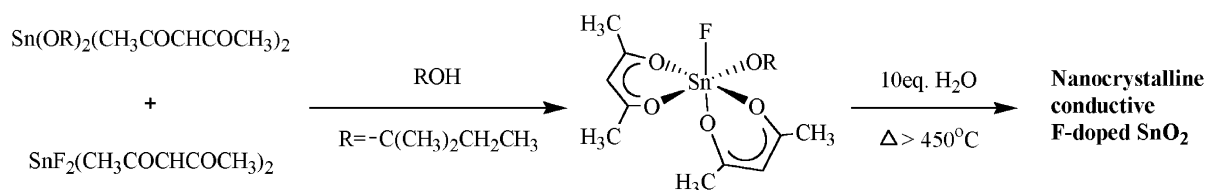
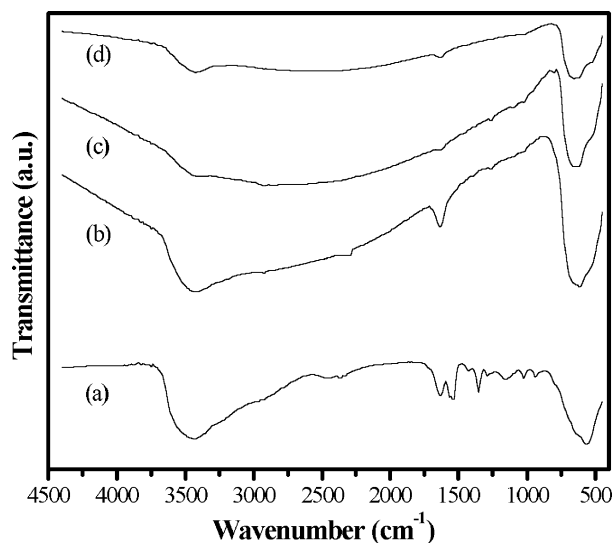Fig. 1. Synthetic route used to prepare nano-crystalline F-doped SnO_2

Fig. 3. FT-IR spectra of F-doped SnO_2 samples calcined at different temperatures. (a) 80 °C, (b) 450 °C, (c) 550 °C, (d) 650 °C.

Table 1
Chemical composition of the samples prepared (from elemental analysis)

Sample	Chemical composition
G^{80}	$SnF_{0.8}(OH)_{0.8}O_{1.1}(C_5H_7O_2)_{0.2} \cdot 0.8H_2O$
G^{450}	$SnO_{2.9}F_{0.08}C_{0.06}$
G^{550}	$SnO_{2.8}F_{0.02}C_{0.03}$
G^{650}	$SnO_{2.2}F_xC_x$ ($x < 0.005$)

After treatment at 650 °C, fluorine and carbon only existed as traces.

The BET surface area, total pore volume and mean pore size (BJH model) results are shown in Fig. 4 and summarized in Table 2. The xerogel G^{80} exhibits a specific surface area of $215 \, m^2 \, g^{-1}$, and a total pore volume of $0.19 \, cm^3 \, g^{-1}$. A strong decrease of the specific surface area occurred upon annealing concomitant with a slight increase of the total pore volume. Indeed, BET surface area was estimated to be 61 and $37 \, m^2 \, g^{-1}$ for G^{550} and G^{650}, respectively, with, in both cases, a total pore volume of $0.23 \, cm^3 \, g^{-1}$. Nitrogen adsorption–desorption isotherms showed a type IV shape with a type H2 hysteresis typical of mesoporous solids prepared by the sol–gel route (Fig. 4) [34]. The hysteresis loop is associated with the filling and emptying of mesopores by capillary condensation and can be related to an interconnected network of pores of different size and shape. After thermal treatment, the mean pore size diameter increased from 60 Å for G^{450} to 240 Å for G^{650}, a drastic change taking place above 450 °C. This behaviour is closely related to the crystallization and sintering of SnO_2 particles as evidenced by XRD measurements.

The structural coarsening observed from the BET and XRD data of tin oxide samples was confirmed by comparing the TEM images of samples calcined between 450 and 650 °C. The TEM image of the xerogel and the calcined F-doped SnO_2 are shown in Fig. 5. The microstructural evolution of the F-doped SnO_2 from 450 to 650 °C indicated an increase in fine structure and was attributed to the growth of nanosized SnO_2 particles. It was clear from Fig. 5(a) that xerogel had "worm-hole" topology with numerous small pores (2–5 nm), this kind of texture being often reported for mesoporous metal oxides [35]. After calcination, this porous structure collapsed and was replaced by a network of aggregated SnO_2 nanoparticles, the size of which rose from 5 to 20 nm as the temperature of heat treatment was increased from 450 to 650 °C for 30 min. At this stage, it is worthwhile to mention that the actual particle size measured from TEM micrographs is larger than that estimated from XRD patterns. It can be rationalized as follows. First of all, the Scherrer formula can lead to an underestimation of the mean crystallite size because the contribution of smaller size components in a crystallite-size distribution governs the width of the XRD lines. In addition, the nanoparticles may contain structural defects, such as twins or macles,
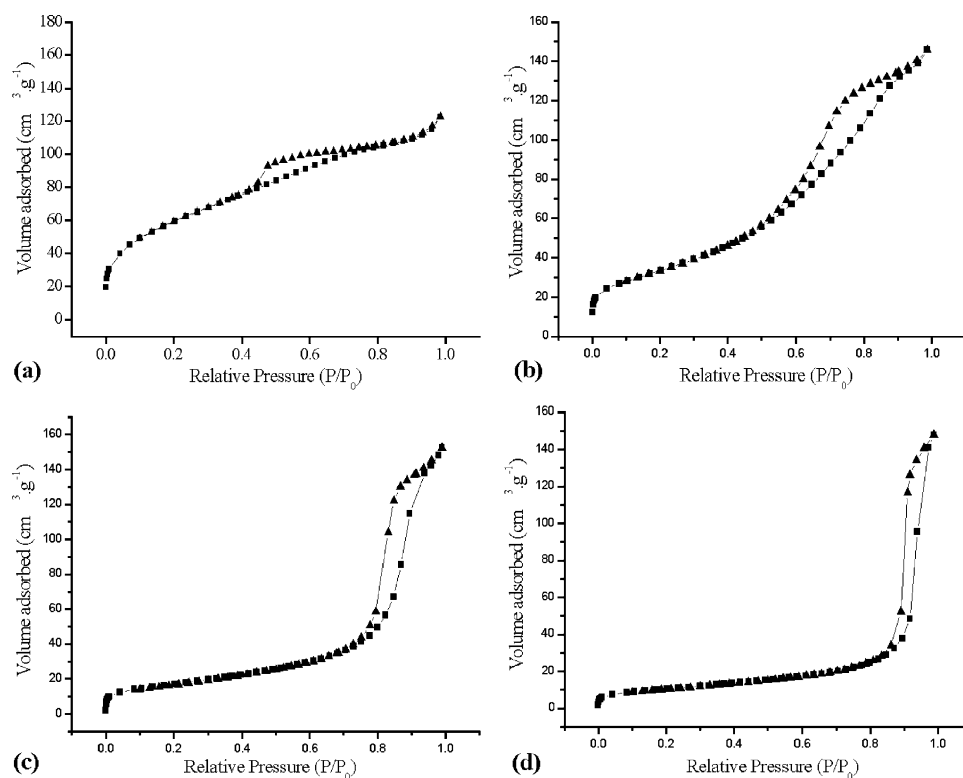
(Space group: $P4_2/mnm$) without any crystalline impurities. These peaks became sharper as the temperature of the thermal treatment was increased that is characteristic of crystallization and particle growth. Thus, average crystallite sizes of about 4, 7 and 11 nm were calculated from the modified Scherrer formula for G^{450}, G^{550} and G^{650}, respectively, which is consistent with the formation of nanocrystalline SnO_2 particles.

The IR spectra of the different samples prepared are depicted in Fig. 3. The sample G^{80} showed a broad resonance assigned to OH stretching modes ranging from ~ 3600 to $2500 \, cm^{-1}$ with a maximum around $3430 \, cm^{-1}$. The water deformation band was detected at $1627 \, cm^{-1}$ and the bands characteristic of acetylacetonato ligands coordinated to tin at 1570 and $1540 \, cm^{-1}$ ($\nu_{sym}(C–O) + \nu_{asym}(C–C)$), 1425 and $1350 \, cm^{-1}$ ($\delta(CH_3)$), 1025 and $945 \, cm^{-1}$ ($\rho(CH_3)$). Finally, the wide bands observed at ~ 647 and $560 \, cm^{-1}$ were attributed to Sn–O–Sn and Sn–O (belonging to Sn–OH groups) stretching vibrations, respectively. After calcination, the main IR features included resonances at ca. 660, 620 and 540 (sh) cm^{-1} which fell into the range of the Sn–O stretching mode region and revealed the complete removal of the chelating ligands.

According to the FTIR experiments and elemental analysis data (Table 1), the formula $SnF_{0.8}(OH)_{0.8}O_{1.1}(C_5H_7O_2)_{0.2} \cdot 0.8H_2O$ may be proposed for G^{80}. This is consistent with the formation of fluorinated oxo-hydroxo tin oligomeric or polymeric structures upon hydrolysis [33], the fluorine amount remaining almost unaffected by the hydrolysis step. After calcination, a dramatic decrease of both fluorine and carbon contents were noted, due to the hydrolysis of the Sn–F bond at high temperature and decomposition of the remaining acetylacetonato ligands. However, doping amount of fluorine (ratio F/Sn = 2–8 at%) in samples G^{450} and G^{550} were obtained.

Fig. 4. Nitrogen adsorption–desorption isotherms of (a) G^{80}, (b) G^{450}, (c) G^{550}, (d) G^{650}.

Table 2
Nitrogen sorption porosimetry studies (BET) of dried and calcined sol–gel samples

Sample	S_{BET} (m²/g)	Total pore volume (cm³/g)	Mean pore diameter (Å)
G^{80}	215	0.19	40
G^{450}	123	0.23	60
G^{550}	61	0.23	130
G^{650}	37	0.23	240

which decreases the size of the monocrystalline domains and, as a result, broadens the XRD peaks.

Fig. 6 shows the first discharge curves of commercial and F-doped SnO_2 electrodes at a current density of 25 mA/g between 1.2 V and 50 mV. In the discharge curves, a plateau at about 1.0 V could be observed for each sample [7]. With the increase of annealing temperature the plateaus became more elongated. After the first cycle, the plateau at about 1.0 V has disappeared in the discharge curves. The discharge curves were similar to that reported by Courtney and Dahn [7]. For each sample, high irreversible capacities of the working electrode were observed during the initial discharge likely due to the formation of Li_2O. At the same discharge capacity, F-doped SnO_2 electrode showed higher discharge voltage than commercial SnO_2 electrode. A higher insertion voltage can be observed at the same insertion level for an n-type semiconducting electrode with

smaller particles; moreover, the potential decreased more smoothly as the lithium-insertion progressed in these kinds of electrodes composed of nanocrystalline materials [36]. The capacity retention characteristics of the F-doped SnO_2 and commercial SnO_2 electrode in the voltage range 50 mV–1.2 V (vs. Li/Li^+) are shown in Fig. 7. The initial and second discharge capacities of the F-doped and commercial SnO_2 and capacity retention ratio are summarized in Table 3. The capacity of SnO_2 is calculated capacity of composite divided by the SnO_2 weight fraction. The nanocrystalline F-doped SnO_2 electrodes studied in this report clearly exhibited a better capacity retention compared to the commercial SnO_2 electrodes. The initial discharge capacity (1775, 1814, 1922 mA h/g) of the G^{450}, G^{550} and G^{650} electrodes increased as the annealing temperature was risen, and was significantly higher than that found for the commercial SnO_2 electrode (1311 mA h/g). Furthermore, G^{450}, G^{550} and G^{650} electrodes exhibited capacity of 560, 502, and 702 mA h/g with 48%, 50%, and 40% capacity retention after 25 cycles between 1.2 V and 50 mV at the rate of 25 mA/g, respectively. It is also worthwhile to mention that the irreversible capacity of the F-doped SnO_2 electrodes was relatively small compared to the commercial SnO_2 electrode. As shown in Fig. 7, the discharge capacity of commercial SnO_2 dramatically decreased to 90 mA h/g after 25 cycles with retention ratio of 23%, whereas those of the G^{450}, G^{550} and G^{650} electrodes showed relatively better capacity retention. The origin of these disparate electrochemical performances
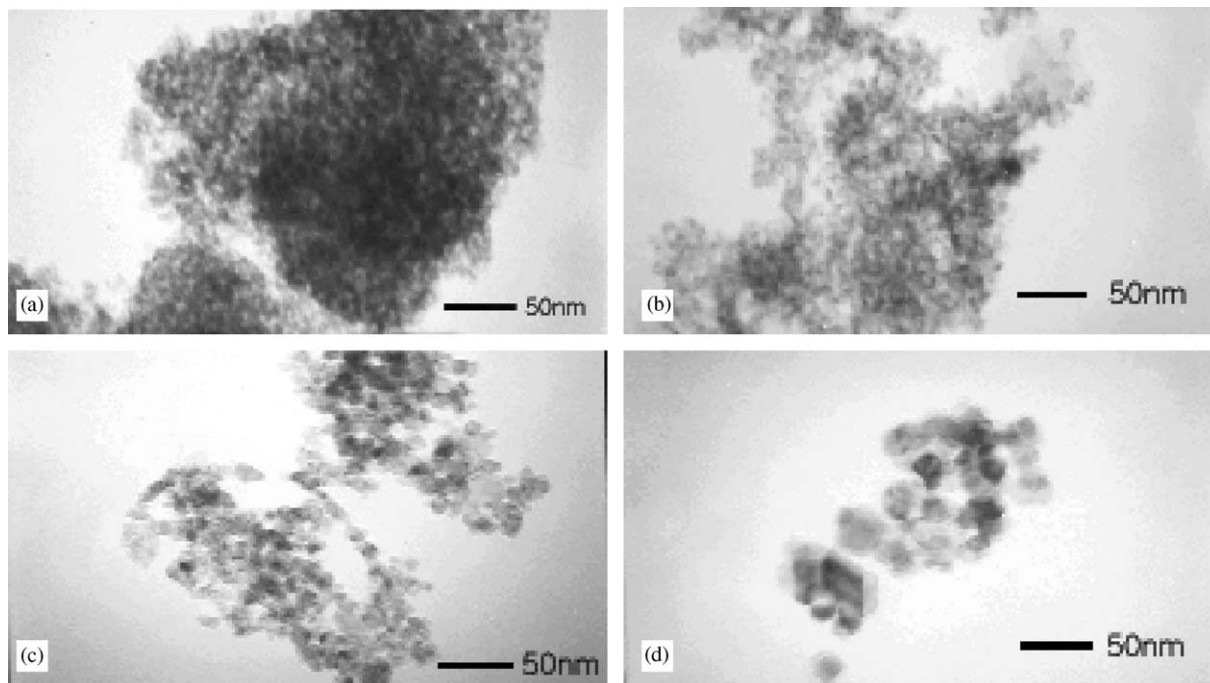
Fig. 5. Transmission electron micrographs of (a) G^{80}, (b) G^{450}, (c) G^{550}, (d) G^{650}.
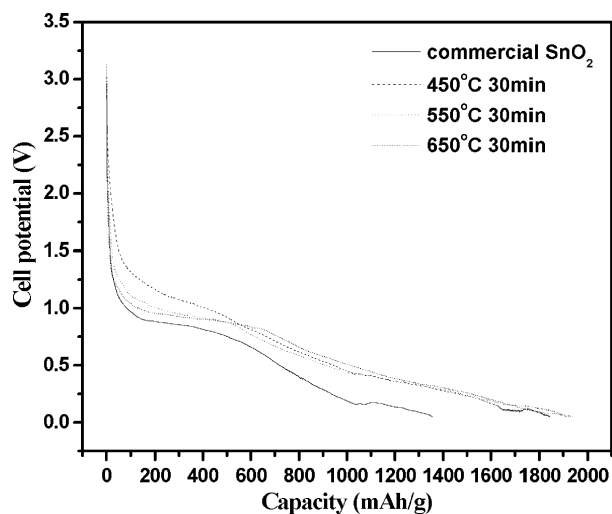

Fig. 6. First discharge curves of the undoped and F-doped SnO_2 at a rate of 25 mA/g between 1.2 V and 50 mV.

Fig. 7. Comparison of cycleability of undoped and F-doped SnO_2 anode between 1.2 V and 50 mV.

still remains unclear, however it seems that a mesoporous nanocrystalline and conductive matrix facilitates the diffusion of Li and the dispersion of tin atoms in the electrodes [16]. Further experimental work is currently in progress to improve our understanding of the structural and electrical properties of F-doped materials.

4. Conclusions

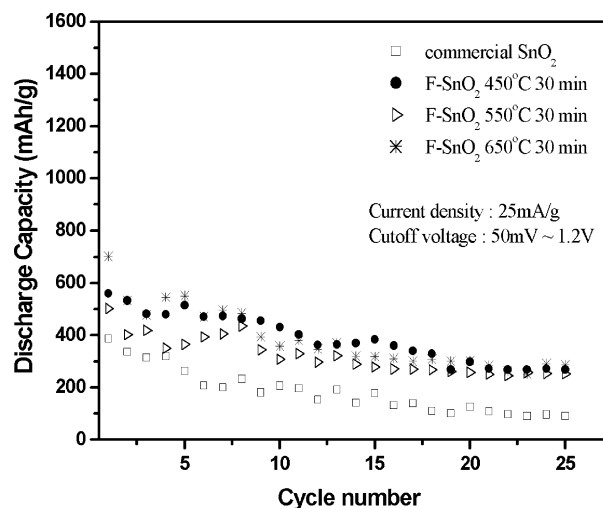Fluorine-doped nanocrystalline SnO_2 materials have been successfully synthesized by the sol–gel route from a single molecular precursor followed by a heat-treatment at 450–650 °C. The calcination step gave rise to a porous network of aggregated nanoparticles. The mean particle size of the F–SnO_2 materials increased from 5 to 20 nm and the specific surface area decreased from 123 to 37 m^2/g as the temperature of heat treatment was risen from 450 to 650 °C. The F-doped SnO_2 electrode showed higher reversible and smaller irreversible capacity than commercial SnO_2 electrode between 1.2 V and 50 mV at the rate of 25 mA/g. An improvement of the capacity retention of the

Table 3
Initial and after 25 cycle discharge capacities and capacity retention ratios of F-doped SnO_2 and commercial SnO_2

Samples	Initial discharge capacity (mA h/g)	Initial charge capacity (mA h/g)	Second discharge capacity (mA h/g)	After 25 cycle discharge capacity (mA h/g)	Capacity retention ratio (%)
Commercial SnO_2	1311	367	388	90	23
G^{450}	1775	619	560	268	48
G^{550}	1814	575	502	252	50
G^{650}	1922	733	702	287	40

F-doped SnO_2 electrode could be obtained by the proper synthetic design of nanocrystalline active material.

Acknowledgements

References

[1] T. Miyasaka, T. Watanabe, A. Fujishima, K. Honda, Nature 277 (1979) 836.
[2] H. Ogawa, A. Abe, M. Nishikawa, S. Hayakawa, J. Electrochem. Soc. 128 (1981) 2020.
[3] S. Shukla, S. Patil, S.C. Kuiry, Z. Rahamn, T. Du, L. Ludwig, C. Parish, S. Seal, Sensors Actuators B 96 (2003) 343.
[4] H. Cachet, V. Vivier, T. Toupance, J. Electroanal. Chem. 572 (2004) 249.
[5] O.K. Varghese, L.K. Malhotra, Sensors Actuators B 53 (1998) 19.
[6] S. Ferrere, A. Zaban, B.A. Gregg, J. Phys. Chem. 101 (1997) 4490.
[7] I.A. Courtney, J.R. Dahn, J. Electrochem. Soc. 144 (1997) 2045.
[8] R.A. Huggins, Ionics 3 (1997) 245.
[9] Y. Wang, J.Y. Lee, J. Phys. Chem. 108 (2004) 17832.
[10] Y. Wang, J.Y. Lee, J. Power Sources 144 (2005) 220.
[11] J. Morales, L. Sanchez, J. Electrochem. Soc. 146 (1999) 1640.
[12] T. Maruyama, K. Tabata, J. Appl. Phys. 68 (1990) 4282.
[13] J.-H. Ahn, G.X. Wang, J. Yao, H.K. Liu, S.X. Dou, J. Power Sources 119–121 (2003) 45.
[14] J. Read, D. Foster, J. Wolfenstine, W. Behl, J. Power Sources 96 (2001) 277.
[15] J. Bruneaux, H. Cachet, M. Froment, A. Messad, Electrochim. Acta 39 (1994) 1251.
[16] C.W. Kwon, G. Campet, J. Portier, A. Poquet, L. Fournes, C. Labrugere, B. Jousseaume, T. Toupance, J.H. Choy, M.A. Subramanian, Int. J. Inorg. Mater. 3 (2001) 211.
[17] K.L. Chopra, S. Major, D.K. Pandya, Thin Solid Films 102 (1983) 1.
[18] J. Zhu, Z. Lu, S.T. Aruna, D. Aurbach, A. Gedanken, Chem. Mater. 12 (2000) 2557.
[19] A.C. Bose, D. Kalpana, P. Thangadurai, S. Ramasamy, J. Power Sources 107 (2002) 138.
[20] D. Aurbach, A. Nimberger, B. Markovky, E. Levi, E. Sominski, A. Gedanken, Chem. Mater. 14 (2002) 4155.
[21] N. Sergent, P. Gelin, L.P. Camby, H. Praliaud, G. Thomas, Sensors Actuators B 84 (2002) 176.
[22] G.H. Philip, C.L. Nicholas, D. Wayne, B. Craig, A. Wan, Chem. Mater. 11 (1999) 896.
[23] J.A. Toledo-Antonio, R. Gutierrez-Baez, P.J. Sebastian, A. Vazquez, J. Solid State Chem. 174 (2003) 241.
[24] Z.X. Deng, C. Wang, Y.D. Li, J. Am. Ceram. Soc. 85 (2002) 2837.
[25] L. Broussous, C.V. Santilli, S.H. Pulcinelli, A.F. Craievich, J. Phys. Chem. B 106 (2002) 2855.
[26] L. Fraigi, D.G. Lamas, N.E.W. Reca, Nanostruct. Mater. 11 (1999) 311.
[27] M. Kakihana, J. Sol–Gel Sci. Technol. 6 (1996) 7.
[28] S. de Monredon, A. Cellot, F. Ribot, C. Sanchez, L. Armelao, L. Gueneau, L. Delattre, J. Mater. Chem. 14 (2002) 2396.
[29] T. Toupance, O. Babot, B. Jousseaume, G. Vilaça, Chem. Mater. 15 (2003) 4691.
[30] A. Gamard, O. Babot, B. Jousseaume, M.C. Rascle, T. Toupance, G. Campet, Chem. Mater. 12 (2000) 3419.
[31] D. Boegeat, B. Jousseaume, T. Toupance, G. Campet, L. Fournes, Inorg. Chem. 39 (2000) 3924.
[32] A. Gamard, B. Jousseaume, T. Toupance, G. Campet, Inorg. Chem. 38 (1999) 4671.
[33] C. Eychenne-Baron, F. Ribot, C. Sanchez, J. Organometal. Chem. 567 (1999) 137.
[34] F. Rouquerol, J. Rouquerol, K. Sing, in: Adsoprtion by Powders & Porous Solids, Academic Press, London, 1999 p. 204.
[35] T.T. Emons, J. Li, L.F. Nazar, J. Am. Chem. Soc. 124 (2002) 8516.
[36] G. Campet, S.J. Wen, S.D. Han, M.C.R. Shastry, J. Portier, C. Guizard, L. Cot, Y. Xu, J. Salardenne, Mater Sci. Eng. B 18 (1993) 201.